The dark neutral medium is (mostly) molecular hydrogen

Harvey Liszt, Maryvonne Gerin

Astronomy & Astrophysics manuscript no. HSL-PMonnier
June 19, 2023

The Dark Neutral Medium is (Mostly) Molecular Hydrogen

H. Liszt[1] and M. Gerin[2]

[1] National Radio Astronomy Observatory, 520 Edgemont Road, Charlottesville, VA, USA 22903 e-mail: hliszt@nrao.edu
[2] LERMA, Observatoire de Paris, PSL Research University CNRS Sorbonne Université
e-mail: maryvonne.gerin@obspm.fr

received June 19, 2023

ABSTRACT

Context. More gas is sometimes inferred in molecular cloud complexes than is represented in HI or CO emission, and this is called dark neutral medium (DNM).
Aims. Our aim is to extend a study of DNM along 13 directions in the outskirts of Chamaeleon by determining the atomic or molecular character of the DNM along a larger sample of sightlines.
Methods. We acquired ALMA ground rotational state absorption profiles of HCO^+ and other molecules toward 33 compact extragalactic continuum background sources seen toward the Galactic anticenter, deriving $N(H_2) = N(HCO^+)/3 \times 10^{-9}$ as before. We observed J=1-0 CO emission with the IRAM 30m telescope in directions where HCO^+ was newly detected.
Results. HCO^+ absorption was detected in 28 of 33 new directions and CO emission along 19 of those 28. The five sightlines lacking detectable HCO^+ have three times lower $<E_{B-V}>$ and <N(DNM)>. Binned in E_{B-V}, $N(H_2)$ and N(DNM) are strongly correlated and vary by factors of 50-100 over the observed range $E_{B-V} \approx 0.05$ - 1 mag, while N(HI) varies by factors of only 2-3. On average N(DNM) and $N(H_2)$ are well matched, and detecting HCO^+ absorption adds little to no H_2 in excess of the previously inferred DNM. There are five cases where $2N(H_2) < N(DNM)/2$ indicates saturation of the HI emission profile. For sightlines with $W_{CO} \geq 1$ K-km s^{-1}, the CO-H_2 conversion factor $N(H_2)/W_{CO} = 2 - 3 \times 10^{20}$ cm^{-2}/(1 K-km s^{-1}) is higher than is derived from studies of resolved clouds in γ-rays.
Conclusions. Our work sampled primarily atomic gas with a mean H_2 fraction $\approx 1/3$, but the DNM is almost entirely molecular. CO fulfills its role as an H_2 tracer when its emission is strong, but large-scale CO surveys are not sensitive to H_2 columns associated with typical values $N(DNM) = 2 - 6 \times 10^{20}$ cm^{-2}. Lower X_{CO} values from γ-ray studies arise in part from different definitions and usage. Sightlines with $W_{CO} \geq 1$ K-km s^{-1} represent 2/3 of the H_2 detected in HCO^+ and detecting 90% of the H_2 would require detecting CO at levels $W_{CO} \approx 0.2$-0.3 K-km s^{-1}.

Key words. interstellar medium – abundances

1. Introduction

Between the atomic and molecular interstellar gases there is a transition that is imperfectly traced in λ21cm HI and/or λ2.6mm CO emission. Gas that is not well represented in one or both tracers is described as dark neutral medium (DNM) (Grenier et al. 2005; Planck Collaboration et al. 2015; Remy et al. 2017, 2018), and the atomic or molecular character of the DNM can only be decided by appealing to other information.

In the outskirts of Chamaeleon, we used millimeter-wave HCO^+ absorption to show that the DNM was almost exclusively molecular, even while the gas as a whole was mostly atomic (Liszt et al. 2018). HCO^+ was detected along all 13 sampled sightlines, of which 12 lacked detectable CO emission at a level of 1.5 K-km s^{-1}. The amount of inferred H_2 was comparable to that of the DNM (confirming the amount of the detected DNM), and only for three sightlines did it seem likely that saturation of the HI emission profile could account for much of the DNM. Subsequent detections of CO absorption along six directions by Liszt et al. (2019) showed that the lack of CO emission was due to low CO column densities. The linewidth of CO absorption was shown to be smaller than that of its parent molecule HCO^+, illustrating the complex chemical nature of the CO formation process in diffuse gas.

Send offprint requests to: H. S. Liszt

In this work we extend the analysis of the composition of DNM to 33 sightlines in directions toward the Galactic anticenter (Remy et al. 2017, 2018) and consider the larger sample of 46 sightlines. The present study employs a relatively small number of diffuse ($A_V \leq 1$ mag) and translucent ($A_V \leq 3$ mag) sightlines where background sources are serendipitously available, and is not a revision of the earlier study, whose derived DNM column densities and other results are assumed here. Rather, we use the newly derived H_2 abundances, independent of the presence of CO emission, to consider such topics as the atomic or molecular character of the DNM, the degree to which the Ł21 HI profile represents N(HI) and the influence of the CO-H_2 conversion factor on the DNM determination.

Section 2 summarizes the observational material considered here and Section 3 compares the prior results for DNM with atomic hydrogen measured in the Ł21 emission and H_2 as sampled by its proxy 89 GHz absorption of HCO^+. The role of CO emission data is explored in Section 4 where the CO-H_2 conversion factor is derived. Section 5 presents a summary, with conclusions and a discussion of later work.

2. Observations and data reduction

The methods of work were described in Liszt et al. (2018) and are not repeated in full detail here. From the existing DNM

analyses of Planck Collaboration et al. (2015) and Remy et al. (2017, 2018) we take N(DNM) and Ł21 HI column densities N(HI) and $N(HI)_{cl}$ representing respectively the line profile integral integrated over all velocities and the column density that is associated with the cloud and/or kinematic features hosting the neutral gas and DNM, as derived by a decomposition that accounts for the compound nature of HI emission profiles from individual clouds.

To the existing analyses we add ALMA observations of absorption from HCO^+ and profiles of λ2.6mm CO emission from the IRAM 30m telescope, as described below.

2.1. Millimeter-wave absorption

The new absorption data discussed here are spectra of HCO^+ in 33 directions along Galactic anticenter sightlines toward ALMA phase calibrators as given in the Tables here and projected on sky maps in Figure 1. As before, the HCO^+ spectra were acquired with a spectral resolution of 0.205 km s^{-1} sampled at 0.102 km s^{-1} intervals without the so-called spectral averaging that bins data. We also acquired spectra of HCN, C_2H, HCO, and several isotopologs. Counts of detections are shown in Figure 2, but results for species other than HCO^+ will be discussed in detail in later work. Statistics of the HCO^+ detections are shown in Figure A.1. Spectra in the 28 directions with detectable HCO^+ absorption are shown in Figure B.1.

2.2. IRAM 30m CO emission

We took frequency-switched CO emission profiles at the IRAM 30m telescope in August 2019 toward the 28 anticenter sightlines with detected HCO^+ absorption. The CO spectra are shown in Figure B.1. These CO data were taken as five-point maps toward the target and displaced by 2 HPBW (2x22″) in the four cardinal directions, using a pointing pattern that was designed to detect HCO^+ and HCN emission in the presence of spectral line absorption in the target direction. For the HCO^+ emission that will be discussed in subsequent work, the HCO^+ emission profile is formed by averaging spectra along the four outlying directions. For CO the present results use the average of all five pointings because contamination by absorption is not measurable given the strength of the emission and/or the continuum. The results are presented on the main beam antenna temperature scale that is native to the 30m telescope.

2.3. Conversion from integrated HCO^+ absorption to $N(H_2)$

The suitability of HCO^+ as a proxy for H_2 in diffuse molecular gas was explored extensively in Liszt & Gerin (2023) (hereafter Paper 1). As in our earlier work, we use $N(H_2) = N(HCO^+)/3 \times 10^{-9}$ and $N(HCO^+) = 1.10 \times 10^{12} \Upsilon_{HCO^+}$ where Υ_{HCO^+} is the integrated HCO^+ optical depth expressed in km s^{-1}.

2.4. Reddening and dust optical depth

The 6′ resolution dust-emission maps scaled to optical reddening E_{B-V} by Schlegel et al. (1998) are cited here. Those reddening values can be converted to Planck 353 GHz dust optical depth using the relationship established by Planck Collaboration et al. (2014) between the 353 GHz dust optical depth and the E_{B-V} values of Schlegel et al. (1998), $E_{B-V}/\tau_{353} = (1.49 \pm 0.03) \times 10^4$ mag.

2.5. Conventions

Velocities presented with the spectra are taken with respect to the kinematic definition of the Local Standard of Rest. N(H) is the column density of H nuclei detected in neutral atomic and molecular form, $N(H) = N(HI)+2N(H_2)$, and the molecular hydrogen and DNM fractions $2N(H_2)/N(H)$ and N(DNM)/N(H) are respectively represented by f_{H_2} and f_{DNM}. The integrated absorption of the HCO^+ profile in units of km s^{-1} is denoted by Υ_{HCO^+} and similarly for other species. The integrated emission of the J=1-0 CO line is denoted by W_{CO} with units of K-km s^{-1} and the CO-H_2 conversion factor $N(H_2)/W_{CO}$ is denoted by X_{CO}. Where reference is made to a typical Galactic or standard CO-H_2 conversion factor, the value $N(H_2)/W_{CO} = 2 \times 10^{20}$ cm^{-2}/(1 K-km s^{-1}) should be understood, as summarized in Table E.1 of Remy et al. (2017).

2.6. Overview

Observational results of importance to this work are given in Table 1 and Table 2, and summaries of mean properties of various subsamples are presented in Table 3. Some statistics of the continuum targets and noise in the detections of HCO^+ absorption are discussed in Appendix A and the CO emission and HCO^+ absorption line profiles are shown in Figure B.1 and discussed in Appendix B.

3. HI, DNM, and H_2 sampled in HCO^+ absorption

Figure 1 shows the new Galactic anticenter sightlines projected on maps of E_{B-V} and N(DNM). The region at $b < -30^o$ is described by Remy et al. (2017) as Cetus, and that at $b > -22^o$ as Taurus-Main. California lies to the north around $b = -10^o$ and Perseus is near (l,b) = 160°,-20°. Taurus-North overlays most of the map region. The individual subregions are not discussed here owing to the sparse sampling.

Counts of sources and detected molecular tracers binned in 0.05 mag intervals of reddening are shown in Figure 2. HCO^+ is the molecular tracer detected most commonly (28 of 33 anticenter sightlines and 41 of 46 overall), followed by C_2H (26 total) and HCN (21 total) . The properties of molecular absorption line tracers other than HCO^+ will be discussed in later work.

The Chamaeleon and Galactic anticenter subsamples have the same mode at E_{B-V} = 0.25 - 0.3 mag in Figure 2, but the anticenter subsample has a high-reddening tail at $E_{B-V} > 0.5$ mag that is absent in Chamaeleon. The Galactic anticenter sample has higher mean extinction and molecular fraction. Overall (see Table 3) the anticenter sources have the following characteristics:

- 33% higher $<E_{B-V}> = 0.36$ vs 0.27 mag;
- Same $<N(HI)> = 1.3 \times 10^{21}$ cm^{-2} and $f_{DNM} = 0.12$;
- 80% higher $<N(HI)_{cl}> = 1.12$ vs 0.62×10^{21} cm^{-2};
- 2 times higher $<2N(H_2)> = 0.80$ vs 0.39×10^{20} cm^{-2};
- 65% higher $f_{H_2} = 0.38$ vs 0.23;
- Higher fraction of detected CO, 9/33 (18/33 in the new work) vs 1/13;
- Higher incidence of nondetection of HCO^+, 5/33 vs 0/13, in some cases due to low flux, see Figure A.1.

The DNM fraction is nearly the same in the two samples (0.12-0.13) and much smaller (0.06) in both subsamples when CO emission was detected at the level of 1 K-km s^{-1}. The DNM fraction is also noticeably smaller when molecular gas sampled in HCO^+ absorption is absent, and similarly at $E_{B-V} < 0.2$ mag. The strongest variations in f_{DNM} in Table 3 arise in selections

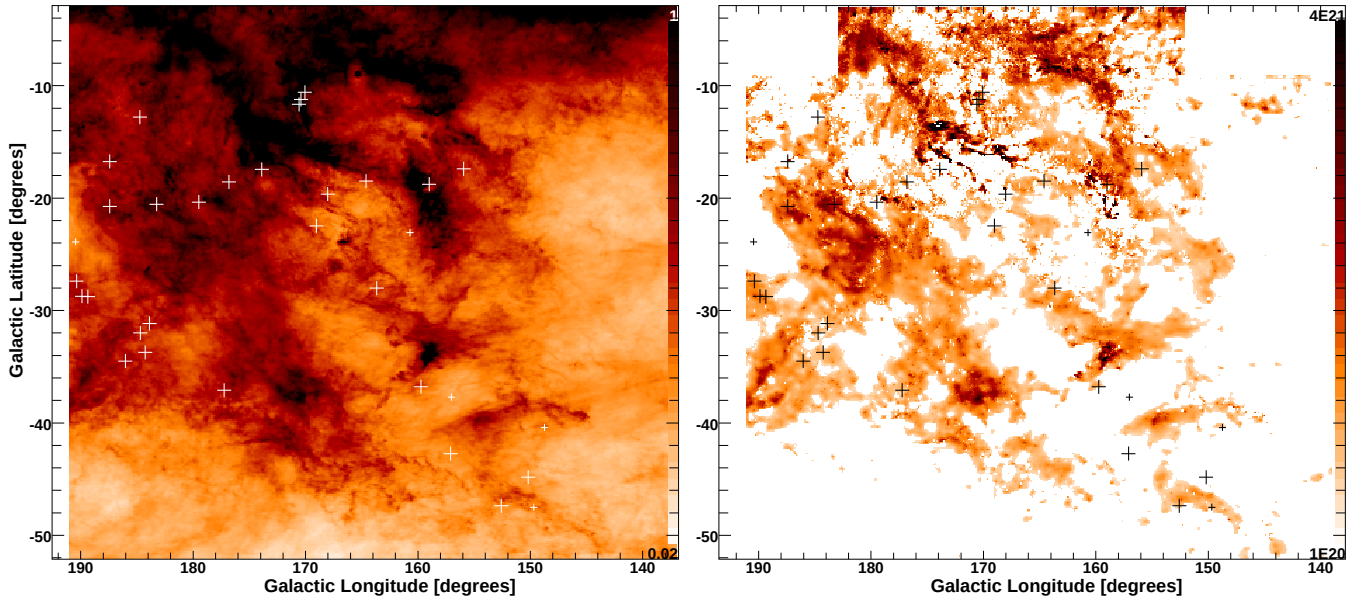

Fig. 1. Sky maps of the observed sightlines. Left: Positions of the background sources observed here are projected against a map of E_{B-V} from the work of Schlegel et al. (1998). The sightlines lacking detected HCO^+ absorption (largely due to weak continuum) are indicated with smaller symbols. Right: Same as left, but shown against a map of N(DNM) from Remy et al. (2017, 2018).

based on the strength of CO emission and are discussed in Section 4.

3.1. Quantitative summary results

Figure 3 shows an overview of trends in means of N(HI), N(DNM), and $N(H_2)$ using data binned in 0.05 mag intervals of reddening as in Figure 2, plotted horizontally at the mean E_{B-V} in every bin. The counts in each bin are shown and the bins at $E_{B-V} > 0.5$ mag are occupied by only one or two sightlines. The association of DNM with molecular gas is unmistakable.

The mean HI column density varies by only a factor of 3 over a wider range E_{B-V} = 0.09 - 1 mag. By contrast, means of N(NDM) and $N(H_2)$ vary by factors of 50-100. The values of $<N(DNM)>$ and $<N(H_2)>$ are comparable and increase steadily for $E_{B-V} \lesssim 0.7$ mag, beyond which $<N(DNM)>$ either fails to increase or falls: the CO emission tracer used to derive N(DNM) was used effectively to account for H nuclei in H_2. The cloud-associated mean $N(HI)_{cl}$ declines at $E_{B-V} \geq 0.7$ mag as H_2 sequesters H nuclei. The value of $<N(H_2)>$ increases up to the bins at highest E_{B-V} where $<N(H_2)> \approx <N(HI>) \approx 2-3\ <N(HI)_{cl}>$ and whole sightlines are dominated by molecular gas.

The correlation between DNM and H_2 is remarkable considering the vastly different scales on which E_{B-V}, N(HI), and N(NDM) are measured (6-20′), as contrasted with $N(H_2) \propto \Upsilon_{HCO^+}$ that is derived on submilliarcsecond scales from absorption against scatter-broadened compact millimeter-wave ALMA calibrator continuum sources. The same kind of correlation of tracers observed on different angular scales occurs in the correlation of integrated λ21cm HI optical depth with E_{B-V} (Liszt 2021).

When HCO^+ is not detected (5/46 directions) the following characteristics are found compared to sightlines with detected HCO^+:

- 3 times lower $<E_{B-V}>$ = 0.13 mag;
- 1.3 times higher $<N(H)>/<E_{B-V}> = 8 \times 10^{21}$ cm^{-2} mag^{-1};
- 3.5 times lower $<N(DNM)> = 8 \times 10^{19}$ cm^{-2};

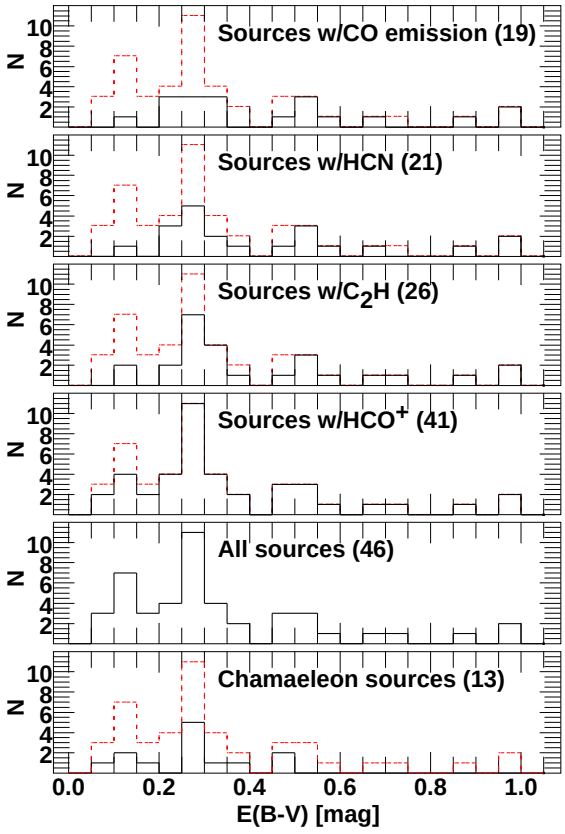

Fig. 2. Counts of sightlines and detected tracers binned in 0.05 intervals of reddening, E_{B-V}. The histogram of all sources is overlaid (dashed red) in the other panels.

- 2 times lower $<f_{DNM}> = 0.07$;
- no DNM in 3/5 cases vs. 15/46 overall.

Instead, using 3σ upper limits for $N(H_2)$ we find:

– >5 times lower $<2N(H_2)> \leq 1.5 \times 10^{20}$ cm^{-2} and
– >2.5 times lower $<f_{H_2}> \leq 0.14$

The ensemble of sightlines with N(DNM) < 5×10^{19} cm^{-2} does not differ by more than 10-20% from other sightlines in any mean property not involving N(DNM). The variations in N(DNM) and N(H_2) stand in great contrast with N(HI) that increases only by a factor of 3 across the figure. The rise in N(H_2) accounts for the failure of N(HI) to increase at high E_{B-V}, but this could in principle also be explained by increasing saturation of the HI emission. As noted in Planck Collaboration et al. (2015) and further refined by Remy et al. (2018), the global DNM analysis finds the best fit with the optically thin estimate of N(HI), implicitly leaving a bigger overall role for molecular gas than for saturation of the HI profile.

3.2. DNM and HI

Shown in Figure 4 is the variation of <N(DNM)> with <N(HI)> and $<N(HI)_{cl}>$. Chamaeleon differs from the Galactic anticenter in having more extraneous atomic gas along the line of sight and smaller values of cloud-associated gas. The cloud-associated HI in Chamaeleon is clustered at the low end of the range, even though the samples are evenly matched in the span of their total HI column density and have the same mean N(HI) in Table 3.

Sightlines lacking DNM are present at all N(HI), but N(DNM) is uniformly small along sightlines at the highest column densities N(HI) $\gtrsim 2.3 \times 10^{21}$ cm^{-2} where CO emission is more commonly observed. The sources with N(DNM) > 6×10^{20} cm^{-2} and high N(DNM)/N(HI) ratios are perhaps the most obvious candidates for hosting significant quantities of DNM in atomic form as the result of saturation of the HI profile, but only two of these actually have small contributions from N(H_2). Assessing the DNM contribution arising from possible saturation of the HI profile is discussed in Section 3.3 where it is seen that the strongest cases of atomic DNM actually have more modest N(DNM).

3.3. DNM, E_{B-V}, and N(H_2)

As with HI, sightlines lacking DNM are present over the full range of E_{B-V} in Figure 5, top, but they are predominant at smaller N(H_2). Sightlines with $2N(H_2) \lesssim 10^{20}$ cm^{-2} lack DNM. Along sightlines with column densities too low to host molecular gas, the atomic gas is well represented by the optically thin estimates of N(HI) used in the DNM analysis.

Care must be taken in interpreting the relationship of DNM and N(H_2) in Figure 5 because the DNM in part represents material that is missing in the CO emission tracer while some of the H_2 traced by HCO^+ is actually visible in CO emission. To minimize this cross-contamination, Figure 6 shows a plot of N(DNM) vs. N(H_2) for sightlines lacking a detection of CO, using the more sensitive IRAM data for the Galactic anticenter subsample. Included are all but one (12/13) of the Chamaeleon sightlines and 60% of those toward the anticenter.

Sightlines lacking DNM in the absence of CO emission in Figure 6 are almost entirely confined at $2N(H_2) \lesssim 2 \times 10^{20}$ cm^{-2}, so the detections of HCO^+ absorption do not imply much additional gas along sightlines where DNM was not found. Missing from Figure 6 are sightlines with $2N(H_2) \gtrsim 10^{21}$ cm^{-2} corresponding to W_{CO}= 2.5 K-km s^{-1} for the Galactic CO-H_2 conversion factor.

There are two or three cases in each subsample where $N(DNM)/2N(H_2) \gtrsim 2$ and saturation of the Ł21 emission profile may be important. Most of these sightlines have modest values N(DNM) $\approx 4 - 5 \times 10^{20}$ cm^{-2} and are not the sightlines with high N(DNM) that were singled out for discussion in Section 3.2 when comparing N(DNM) and N(HI).

There are also two or three sightlines at N(H_2) > 6×10^{20} cm^{-2} where $N(DNM)/2N(H_2) \lesssim 2$. Overall $<2N(H_2)> = 1.3<N(DNM)>$ for sources lacking CO emission, so H_2 accounts for DNM without adding extra "dark" gas, and the DNM is mostly molecular. As before in Chamaeleon, the DNM is largely molecular, even if the medium overall is predominantly atomic.

4. The role of CO emission

The CO emission that was detected in previous studies used to determine N(DNM) along our sightlines was well above 1 K-km s^{-1} in every case (Table 2), with $<W_{CO}>$ = 4.9K-km s^{-1} (Table 3). This is very nearly the same mean as for the sample of sightlines with $W_{CO} \geq$ 1K-km s^{-1} observed at the IRAM 30m, 5.5 K-km s^{-1} (see Table 2). Compared to the overall average, the sightlines with $<W_{CO}> \geq$ 1K-km s^{-1} have the following characteristics:

– 50-100% higher $<E_{B-V}> = 0.5 - 0.7$ mag;
– 3-4 times higher $<2N(H_2)> = 2 - 3 \times 10^{21}$ cm^{-2};
– 2 times higher $< f_{H_2} > = 0.6$;
– 2 times lower $<f_{DNM}> = 0.06$.

The 50% smaller DNM fractions $<f_{DNM}> = 0.06$ along samples of sightlines with $<W_{CO}> \geq$ 1K-km s^{-1} indicate that CO emission is doing a good job of tracing H_2 in gas where the molecular fraction is high (Liszt 2017), CO emission is strong, and the cloud-associated HI fraction declines (Figure 2). However, CO emission in general represents a small portion of the total molecular gas present along the sightlines in this work. For instance, $<2N(H_2)> = 7 \times 10^{20}$ cm^{-2} along 46 sightlines, while $<W_{CO}> \approx 5$ K-km s^{-1} along the 6-10 sightlines where $<W_{CO}> \geq$ 1K-km s^{-1} (Table 3). For a typical Galactic CO-H_2 conversion factor, the summed molecular gas column represented in HCO^+ is three to four times that inferred from the summed CO emission. Most of the molecular gas in our sample was hidden in the DNM prior to our work and is still only revealed by the HCO^+ absorption, even with more sensitve CO observations. The IRAM 30m detections with $<W_{CO}>$ below 1K-km s^{-1} comprise less than 20% of the total amount of CO emission.

4.1. The CO-H_2 conversion factor

Comparison of the scaled HCO^+ absorption and IRAM 30 emission measurements provides the most direct determination of the actual CO-H_2 conversion factor along the lines of sight studied in this work. Figure 7 shows the trends in $<N(H_2)>$, $<W_{CO}>$, and $<N(H_2)>/<W_{CO}>$ binned in 0.05 mag increments of E_{B-V} as in Figure 3. Included are the 28 Galactic anticenter sightlines where HCO^+ was detected, with W_{CO} taken at the 3σ upper limit for sightlines where CO emission was not detected with greater significance. Also included is the sightline toward J1733 in Chamaeleon where CO emission was detected. The 3σ upper limits $W_{CO} \leq 1.5$ K-km s^{-1} in Chamaeleon are not useful.

Figure 7 illustrates the behavior of the CO-H_2 conversion factor that is tabulated for different samples in Table 3. The values of $<N(H_2)>$ and $<W_{CO}>$ both increase steadily with E_{B-V} in Figure 7, but at different rates so that their ratio declines by a factor ≈ 7 to $<N(H_2)>/<W_{CO}> = 2.5 - 3 \times 10^{20} H_2$ cm^{-2}(K-km s^{-1})$^{-1}$ for $E_{B-V} \gtrsim 0.5$ mag. Variations of similar magnitude in

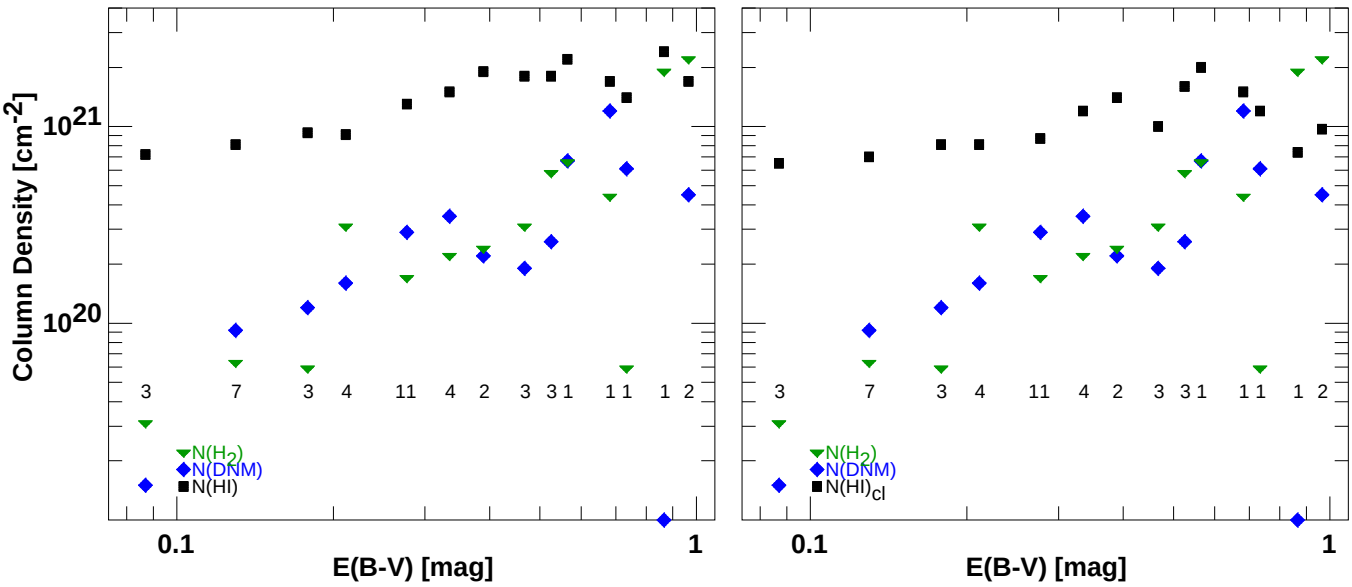

Fig. 3. Trends in mean N(HI), N(H_2), and N(DNM). The results are binned in 0.05 mag intervals of E_{B-V}. Left: N(HI) is calculated over the whole line profile. Right: N(HI) = $N(HI)_{cl}$ the HI column density associated with the clouds studied here. The number of sightlines in each bin is shown in both panels.

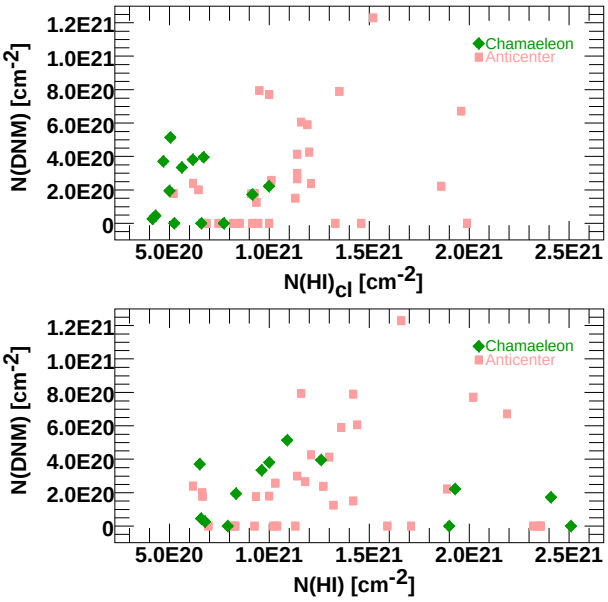

Fig. 4. N(DNM) plotted against total sightline N(HI) (bottom) and cloud-associated atomic hydrogen $N(HI)_{cl}$ (top).

individual diffuse and/or translucent MBM clouds were reported by Magnani et al. (1998) and Cotten & Magnani (2013).

Mean values of $N(H_2)/W_{CO}$ are $2 - 2.5 \times 10^{20} H_2$ cm^{-2}(K-km s^{-1})$^{-1}$ for the old and new samples with $<W_{CO}> \geq 1$ K-km s^{-1}, increasing by factors of 2-3 for the samples with IRAM 30m detections below 1K-km s^{-1} and upper limits. Also see the inset in Figure 7 on this point..

The values of the CO-H_2 conversion factor derived are comparable to those derived in extant Galactic-scale γ-ray analyses (Table E.1 in Remy et al. 2017) when $W_{CO} \gtrsim 1$ K-km s^{-1}, but are uniformly larger than those derived in cloud-level studies like the DNM analysis whose results are summarized in Table 2 of Remy et al. (2017). Those results ranged from $1 - 1.6 \times 10^{20} H_2$ cm^{-2}(K-km s^{-1})$^{-1}$ for determinations based on dust and from $0.44 - 1.00 \times 10^{20} H_2$ cm^{-2} (K-km s^{-1})$^{-1}$ for determinations based on gamma rays.

There is no contradiction with the larger values found in this work whose method of studying widely separated, semi-randomly placed sightlines is similar to the larger scale studies. The strongly CO-emitting ($W_{CO} > 10$ K-km s^{-1}) regions encountered in the cloud-level studies that have generally small values of X_{CO} (see Figure 13 in Remy et al. 2018) were not sampled here.

There may also be a difference arising from the operational definition of the conversion factor. The conversion factors in Table 2 in Remy et al. (2017) are those that optimize the fit of the γ-ray or dust emissivity to a total hydrogen column density that is represented schematically as N(H) = N(HI)+N(DNM)+2N(H_2) = N(HI)+N(DNM)+2$X_{CO}W_{CO}$. After the analysis, there remains a DNM constituent whose molecular fraction is undetermined and not explicitly considered in the definition of the multiplier X_{CO}; we showed that the DNM is largely molecular. By contrast, the present analysis determines N(H_2) independent of CO emission and defines X_{CO} = N(H_2)/W_{CO}. This N(H_2) includes the molecular component of the DNM that we took pains to consider separately in the discussion of Figure 6.

4.2. Achievable limits and detection thresholds for CO, DNM, and H_2

Sightlines in our study often had rms CO emission noise $\Delta W_{CO} \gtrsim 1/3 - 1/2$ K-km s^{-1} in the prior DNM analysis (Table 2). For a typical Galactic conversion $2N(H_2)/W_{CO} = 4 \times 10^{20}$ cm^{-2} (K-kms)$^{-1}$, the equivalent 3σ threshold detection limits on the hydrogen column are $2N(H_2) = 4 - 6 \times 10^{20}$ cm^{-2}, above the actual values of N(DNM) along most of the sightlines we observed. By contrast, the median 3σ detection threshold from HCO^+ in our work is $2N(H_2) > 1.1 \times 10^{20}$ cm^{-2} and typical N(DNM) values are $N(DNM) \gtrsim 2 \times 10^{20}$ cm^{-2} (Figure 6).

The effectiveness of reducing the detection threshold of CO emission below 1 K-km s^{-1} can be assessed by examining the distribution of CO detections and upper limits in the IRAM 30m CO observations. The subsamples of IRAM CO observations

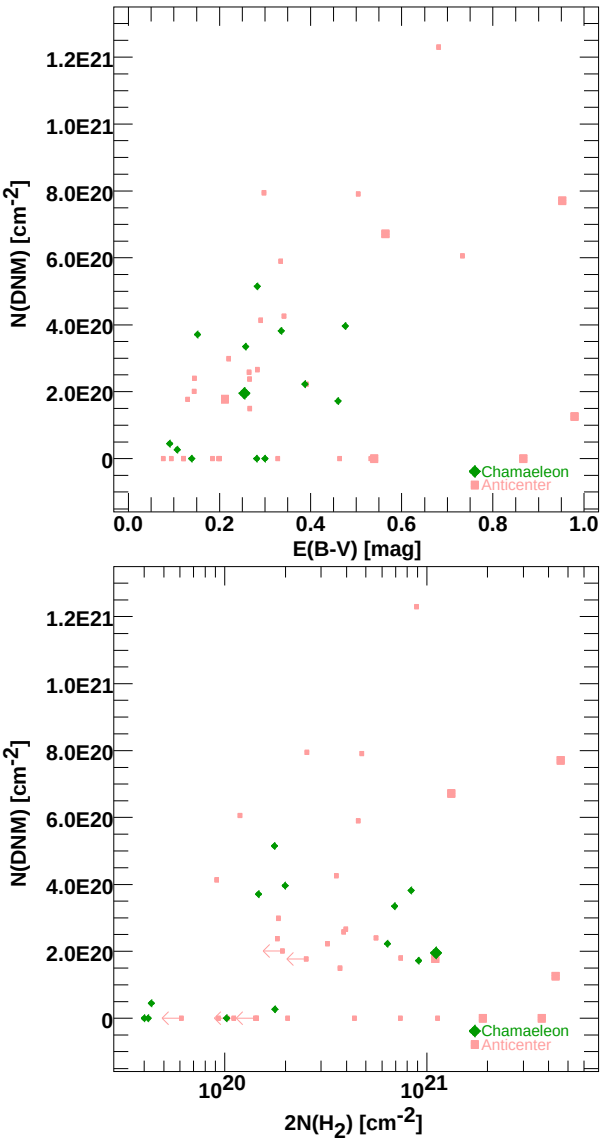

Fig. 5. N(DNM) plotted against E_{B-V} (top) and $2N(H_2)$ (bottom). Larger symbols represent sightlines where $W_{CO} \gtrsim 1$ K-km s^{-1}.

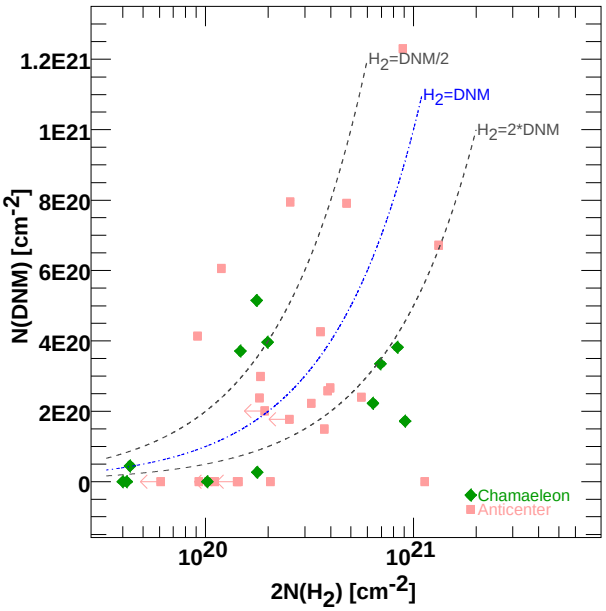

Fig. 6. N(DNM) plotted against $N(H_2)$ for sightlines lacking detected CO emission in the analysis of Remy et al. (2018). Shown are loci at which the number of H nuclei in H_2 is 50, 100, and 200% of that in DNM.

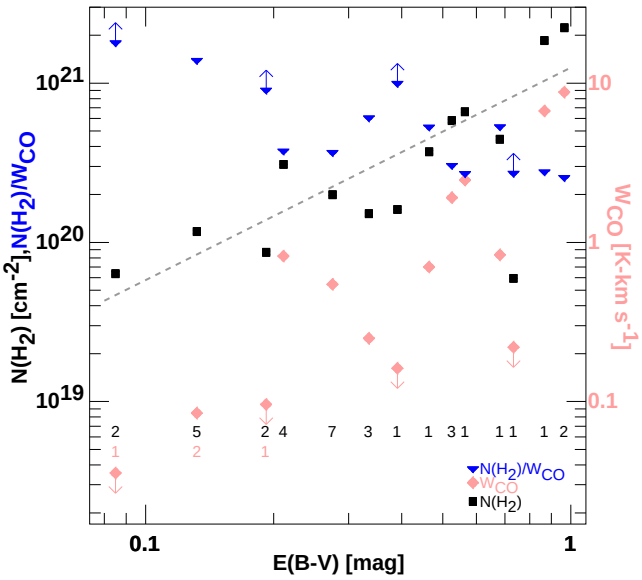

Fig. 7. Trends in mean $N(H_2)$ (black squares), W_{CO} (pink diamonds), and $N(H_2)/W_{CO}$ (blue triangles). The results are binned in 0.05 mag intervals of E_{B-V}, as in Figure 3. Bins in which all sightlines have only upper limits on W_{CO} are indicated by upper and lower limits. The scales for $N(H_2)$ cm^{-2} and $N(H_2)/W_{CO}$ (cm^{-2} (K-km s^{-1})$^{-}$1) are read on the left vertical axis and that for W_{CO} (K-km s^{-1}) on the right. The number of sightlines in each bin is shown as in Figure 3 and the count is carried separately for W_{CO} at low E_{B-V}. The light gray dashed line is a power-law fit $N(H_2) = 10^{21.0973} E_{B-V}{}^{1.335}$.

summarized in Table 3 show 6 detections with $W_{CO} > 1$ K-km s^{-1}, 12 detections with $W_{CO} < 1$ K-km s^{-1}, and ten upper limits at levels $W_{CO} < 0.1 - 0.2$ K-km s^{-1} (see Table 1 for values of upper limits and Figure 3 for a graphical representation of the data). HCO^+ was detected along all of these sightlines, and the three subsamples respectively represent fractions 0.66, 0.26, and 0.08 of the total amount of H_2.

Thus, a survey with a detection limit of 1 K-km s^{-1} would detect approximately two-thirds of the molecular gas along these diffuse and/or translucent lines of sight, and a much increased effort to reduce the detection limit to 0.2 K-km s^{-1} might find another one-fourth of the H_2. Comparable reductions in the fraction of undetected H_2 with increasing CO sensitivity down to rms levels $\Delta W_{CO} \approx 0.1$ K-km s^{-1} were achieved by Donate & Magnani (2017). Missing one-third of the H_2 at the 1 K-km s^{-1} threshold is consistent with the dark gas fraction derived by Wolfire et al. (2010) and Gong et al. (2018).

4.3. The wider view

In Section 4.2 we note that two-thirds of the H_2 was found along the sightlines with $W_{CO} > 1$ K-km s^{-1} and that a deeper survey with a detection limit of 0.2 K-km s^{-1} would have found another 25% of the H_2. At this point we can ask how the results of this sparse sampling are reflected in the region as a whole. We drew a hull around the observed anticenter sightlines, as shown in Fig-

ure C.1 and derived the pixel-by-pixel statistics for the contained area, the amount of material (taken proportional to E_{B-V}), and the amount of H_2. For H_2 we used the $N(H_2)$-E_{B-V} relationship $N(H_2) = 10^{21.0973} E_{B-V}{}^{1.335}$ [1] and the fact that $W_{CO} \gtrsim 1$ K-km s^{-1} at $E_{B-V} \gtrsim 0.4$ mag or $N(H_2) \gtrsim 4 \times 10^{20}$ cm^{-2} in Figure 7 (see also Figure 5 of Paper 1).

Figure 8 shows the probability densities (at left) and cumulative distributions for the derived quantities. Reading values off the cumulative probability distributions at right in Figure 8, conditions with $E_{B-V} \geq 0.4$ mag, $N(H_2) \gtrsim 4 \times 10^{20}$ cm^{-2} occur over one-fourth of the total area containing one-half of the total projected gas column and two-thirds of the H_2. Apparently, the sampled sightlines were representative of the region as a whole regarding the H_2 distribution.

Sampling 90% of the H_2 would require detecting CO emission at $E_{B-V} \gtrsim 0.2$ mag where $N(H_2) \approx 2 \times 10^{20}$ cm^{-2}. The sampling here is too sparse to derive an equivalent value of W_{CO} in Figure 7, but the broader sample in Paper 1 suggests $W_{CO} \gtrsim 0.3$ K-km s^{-1} would be appropriate. Sightlines with $E_{B-V} < 0.32$ mag or $A_V < 1$ mag comprise two-thirds of the area, one-third of the mass, and one-fourth of the H_2.

4.4. Comparison with predictions and models

For models, the critical factors in predicting the amount of dark gas are the threshold where W_{CO} reaches the 1 K-km s^{-1} brightness level and the amount of material above the threshold. In the regime of diffuse molecular gas the integrated brightness of the J=1-0 line is determined almost exclusively by the CO column density, with W_{CO} (K-km s^{-1}) = $N(CO)/10^{15}$ cm^{-2} for hydrogen number densities $n(H) = 64 - 500$ cm^{-3} (Liszt 2007, 2017; Hu et al. 2021) and kinetic temperatures appropriate to the local thermal pressure. This simple proportionality between column density and brightness persists well beyond the CO column density where the J=1-0 transition becomes optically thick, owing to the strongly subthermal excitation (Goldreich & Kwan 1974).

Thus, the CO chemistry dominates the CO brightness, and the sky map of CO emission is a map of the chemistry. The observations can be reproduced by an ad hoc CO formation chemistry in which a fixed relative abundance of HCO^+ $N(HCO^+)/N(H_2) = 3 \times 10^{-9}$ thermally recombines to CO if the H_2 formation and shielding of H_2 and CO are treated self-consistently along with the heating and cooling Liszt (2017). However, networks of chemical reactions in quiescent gas may fail to form the observed quantity of HCO^+ and produce too little CO. This causes the CO brightness to reach 1 K-km s^{-1} at overly large values of E_{B-V} and $N(H_2)$ where shielding of CO by dust and H_2 make up for the deficit in the CO formation rate (e.g., Gong et al. 2018 Figure 7; Hu et al. 2021 Figure 9).

Models with a weak CO formation chemistry have an innate tendency to overestimate the amount of CO-dark gas, but the actual amount of CO-dark gas depends on the distribution of material. In practice the DNM fraction seen by Remy et al. (2018) varied from 0 to 0.3 (their Figure 8) and the sightlines sampled here had $<f_{DNM}> = 0.13$.

5. Summary

We took 89.2 GHz ALMA HCO^+ absorption spectra toward 33 compact millimeter-wave extragalactic continuum sources seen against the Galactic anticenter (Figure 1 and the tables above). We also observed J=1-0 CO emission at the IRAM 30m telescope in the 28 anticenter directions where HCO^+ was detected. Inferring $N(H_2)$ from $N(HCO^+)$ using the ratio $N(HCO^+)/N(H_2) = 3\times10^{-9}$, we combined these results with those from our earlier study of 13 directions where HCO^+ absorption was detected in the outskirts of Chamaeleon. We compared the inferred $N(H_2)$ with prior determinations of the column densities of the dark neutral medium, the neutral gas of uncertain (atomic or molecular) character that had been found to be missing in HI and/or CO emission when compared with the submillimeter dust and γ-ray emissivities of large-scale molecular cloud complexes.

Binning the HI, H_2, and DNM column densities in reddening, we showed in Figure 3 that the mean DNM and molecular gas column densities were comparable and varied compatibly by factors of 50-100 over the observed range $E_{B-V} = 0.09$ - 1 mag, while N(H(I) varied by only factors of 2-3. The means of $N(H_2)$ and N(DNM) are small at low mean reddening, and increase in similar fashion up to $E_{B-V}= 0.5$ mag where molecular gas begins to dominate and CO emission is strong. $N(H_2)$ continues to increase with higher reddening, but N(DNM) and the column density of cloud-associated HI fall where H_2 dominates (sequestering hydrogen) and CO emission is stronger and more closely representative of $N(H_2)$.

We made detailed individual sightline-level comparisons of N(DNM) with E_{B-V}, N(HI), and $N(H_2)$ in Figures 4-6. Sightlines with appreciable DNM appear at all N(HI) (Figure 4); the overall mean DNM fraction $f_{DNM} = N(DNM)/(N(HI)+2N(H_2)) = 0.12$ is modest. Sightlines with appreciable DNM are lacking when $E_{B-V} \lesssim 0.15$ mag (Figure 5) and when $2N(H_2) \lesssim 10^{20}$ cm^{-2} or $2N(H_2) \gtrsim 10^{21}$ cm^{-2} (Figure 6). In Figure 6 we compared N(DNM) and $N(H_2)$ in directions lacking detected CO emission in order to eliminate the case that H_2 was already represented by CO emission in the DNM analysis. This figure showed that there were 2-3 sightlines in each subsample (Chamaeleon and anticenter) or 5-6/46 overall where $2N(H_2) <\leq N(DNM)/2$ and H_2 accounted for the minority of the DNM. There are also a few directions at $2N(H_2) \approx 10^{21}$ cm^{-2} where $2N(H_2) > 2N(DNM)$. Overall, the amounts of DNM and H_2 are similar $<2N(H_2)> = 1.3 <N(DNM)>$ for the unambiguous cases lacking CO emission. The form of the DNM is overwhelmingly molecular hydrogen.

Directions with $<W_{CO}> >1$ K-km s^{-1} have two times smaller mean DNM fractions $<f_{DNM}> = 0.06$, while sightlines with $<W_{CO}> < 1$ K-km s^{-1} have three times higher $f_{DNM} \gtrsim 0.17$-0.19 (Table 3). The relatively few sightlines with $W_{CO} \geq 1$ K-km s^{-1} contain two-thirds of the H_2 detected in HCO^+, and detecting 90% of the H_2 would require detecting CO at levels $W_{CO} \approx 0.2$-0.3 K-km s^{-1}.

The CO-H_2 conversion factor falls steadily with increasing E_{B-V} or W_{CO} in Figure 7. Because the H_2 is concentrated in the sightlines with $W_{CO} \geq 1$ K-km s^{-1}, the overall mean CO-H_2 conversion factors in our work are $<N(H_2)>/<W_{CO}> = 2 - 3 \times 10^{20} H_2$ cm^{-2} for samples of sightlines with detectable CO emission. These values are comparable to previously determined large-scale Galactic averages, and are substantially higher than the global values determined by the cloud-level analyses quoted here to derive N(DNM). We ascribed these differences in part to the present sampling of widely scattered sightlines (i.e., that we did not do a cloud-level analysis) and perhaps to differences in the operational definition of the conversion factor, as discussed in Section 4.1.

Subsequent papers derived from the observations discussed here will focus on the physics and chemistry of the molecules

[1] $f_{H_2} = 2N(H_2)/N(H) = 0.4$-0.5 at $E_{B-V} = 2$ mag if $N(H)/E_{B-V} = 6 - 8 \times 10^{21}$ mag^{-1}

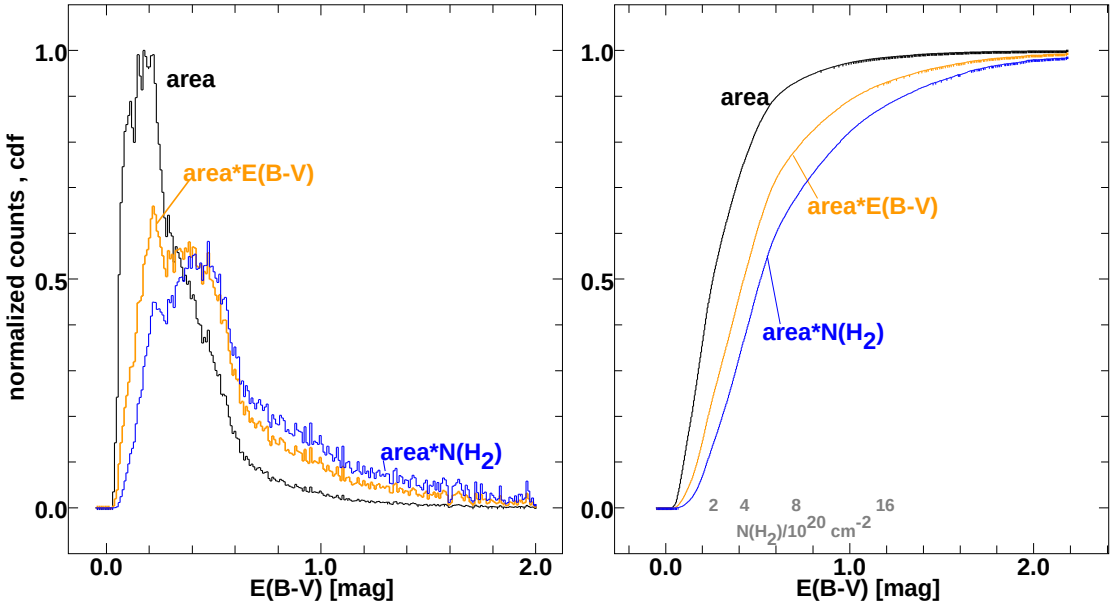

Fig. 8. Probability distributions of area, amount of material, and molecular hydrogen with respect to E_{B-V}. Left: Counts (probability density) scaled to the same area. Right: Cumulative distribution function. $N(H_2)$ is calculated using the mean power-law fit $N(H_2) = 10^{21.0973} E_{B-V}^{1.335}$ derived as shown in Figure 7.

Table 1. Line-of-sight properties and new results for HCO^+ and CO

Source	RA(J2000)	Dec(J2000)	l	b	E_{B-V}[1]	89 GHz flux	Υ_{HCO^+}[2]	$\sigma\Upsilon_{HCO^+}$[3]	W_{CO}[4]	σW_{CO}[5]
	hh.mmsss	dd.mmsss	degrees	degrees	mag	Jy	km s^{-1}	km s^{-1}	K-km s^{-1}	K-km s^{-1}
J0203+1134	2.03464	11.34492	149.6826	-47.4992	0.144	0.126	≤0.263	0.088		
J0209+1352	2.09357	13.52045	150.1800	-44.8290	0.094	0.223	0.20	0.050	≤0.071	0.024
J0211+1051	2.11132	10.51348	152.5781	-47.3674	0.145	0.462	0.76	0.029	0.36	0.025
J0213+1820	2.13105	18.20255	148.7289	-40.4014	0.130	0.093	≤0.345	0.115		
J0231+1322	2.31459	13.22547	157.0917	-42.7380	0.121	0.430	0.14	0.025	≤0.064	0.021
J0242+1742	2.42243	17.42589	157.0180	-37.7033	0.077	0.227	≤0.151	0.050		
J0252+1718	2.52077	17.18427	159.7420	-36.7885	0.220	0.172	0.25	0.077	≤0.096	0.032
J0325+2224	3.25368	22.24004	163.6700	-28.0213	0.213	1.162	1.01	0.017	0.94	0.051
J0329+3510	3.29154	35.10060	155.9152	-17.4042	0.267	0.570	0.51	0.032	≤0.143	0.048
J0329+2756	3.29577	27.56155	160.7030	-23.0743	0.198	0.158	≤0.193	0.064		
J0334+0800	3.34533	8.00144	177.2396	-37.0871	0.391	0.150	0.44	0.088	≤0.162	0.054
J0336+3218	3.36301	32.18293	158.9998	-18.7650	0.733	1.689	0.16	0.009	≤0.219	0.073
J0356+2903	3.56085	29.03423	164.6120	-18.4927	0.212	0.139	1.50	0.090	1.62	0.042
J0357+2319	3.57216	23.19538	169.0302	-22.4661	0.185	0.224	0.28	0.027	≤0.192	0.064
J0400+0550	4.00117	5.50431	184.2710	-33.7266	0.266	0.159	0.25	0.063	≤0.172	0.057
J0401+0413	4.01199	4.13344	186.0261	-34.4947	0.341	0.405	0.49	0.021	0.19	0.048
J0403+2600	4.03056	26.00015	168.0260	-19.6483	0.201	0.331	0.60	0.029	0.62	0.067
J0406+0637	4.06343	6.37150	184.7075	-32.0009	0.283	0.264	0.54	0.051	0.63	0.040
J0407+0742	4.07291	7.42075	183.8723	-31.1558	0.265	0.387	0.53	0.031	0.19	0.042
J0426+0518	4.26366	5.18199	189.3631	-28.7705	0.291	0.516	0.12	0.020	≤0.170	0.057
J0426+2327	4.26557	23.27396	173.8881	-17.4457	0.539	0.304	2.57	0.057	4.84	0.045
J0427+0457	4.27476	4.57083	189.8857	-28.7306	0.335	0.414	0.62	0.024	0.39	0.045
J0437+2037	4.31038	20.37343	176.8096	-18.5565	0.532	0.217	1.54	0.073	0.67	0.026
J0431+1731	4.31574	17.31358	179.4942	-20.3579	0.464	0.104	1.01	0.110	0.70	0.049
J0433+0521	4.33111	5.21156	190.3730	-27.3967	0.298	4.911	0.35	0.003	≤0.109	0.036
J0437+2940	4.37044	29.40138	170.5818	-11.6609	0.979	0.059	5.92	1.138	10.42	0.027
J0438+3004	4.38049	30.04455	170.4116	-11.2283	0.952	0.689	6.25	0.038	7.11	0.026
J0439+3045	4.39178	30.45076	170.0655	-10.5913	0.867	0.195	5.05	0.082	6.69	0.027
J0440+1437	4.40211	14.37570	183.2538	-20.5438	0.681	0.337	1.21	0.031	0.83	0.029
J0445+0715	4.45014	7.15539	190.4535	-23.8898	0.121	0.275	≤0.083	0.028		
J0449+1121	4.49077	11.21286	187.4274	-20.7365	0.504	0.521	0.65	0.022	0.23	0.033
J0502+1338	5.02332	13.38110	187.4143	-16.7456	0.564	0.271	1.81	0.059	2.46	0.031
J0510+1800	5.10024	18.00416	184.7304	-12.7895	0.328	2.411	0.13	0.005	0.17	0.036

[1]From Schlegel et al. (1998)
[2]Integrated optical depth or 3σ upper limit over a 3 km s^{-1} interval
[3]Integrated emission from our results or 3σ upper limit over a 3 km s^{-1} interval
[4] rms of detected emission or rms over a 3km s^{-1} interval

Table 2. Line-of-sight properties and derived quantities

Source	E(B-V)	N(HI)[1]	$N(HI)_{cl}$[1]	$2N(H_2)$ [2]	W_{CO}[3]	N(DNM) [1]	$2N(H_2)/N(HI)$	N(DNM)/N(HI)	X_{CO}[4]
	mag	10^{21} cm^{-2}	10^{21} cm^{-2}	10^{21} cm^{-2}	K-km s^{-1}	10^{21} cm^{-2}			
J0203+1134	0.144	0.664	0.646	≤0.193		0.201	≤0.290	0.303	
J0209+1352	0.094	0.696	0.686	0.144		0.00	0.206	0.00	
J0211+1051	0.145	0.618	0.617	0.561		0.240	0.908	0.388	
J0213+1820	0.130	0.933	0.911	≤0.253		0.177	≤0.271	0.190	
J0231+1322	0.121	0.926	0.852	0.103		0.00	0.111	0.00	
J0242+1742	0.077	0.820	0.819	≤0.111		0.00	≤0.135	0.00	
J0252+1718	0.220	1.142	1.139	0.184		0.299	0.161	0.262	
J0325+2224	0.213	0.999	0.926	0.742	2.82	0.180	0.743	0.180	1.314
J0329+3510	0.267	1.418	1.131	0.372		0.150	0.263	0.106	
J0329+2756	0.198	1.129	1.002	≤0.142	≤ 1.97	0.00	≤0.126	0.00	
J0334+0800	0.391	1.893	1.855	0.322		0.223	0.170	0.118	
J0336+3218	0.733	1.435	1.165	0.119	≤2.60	0.606	0.082	0.423	
J0356+2903	0.212	0.666	0.520	1.099	1.40	0.178	1.650	0.267	3.931
J0357+2319	0.185	1.022	0.944	0.205	≤0.79	0.00	0.200	0.00	
J0400+0550	0.266	1.266	1.210	0.182		0.238	0.144	0.188	
J0401+0413	0.341	1.209	1.202	0.357		0.426	0.296	0.352	
J0403+2600	0.201	0.830	0.667	0.438	1.99	0.00	0.528	0.00	1.101
J0406+0637	0.283	1.182	1.143	0.397		0.266	0.335	0.225	
J0407+0742	0.265	1.033	1.006	0.387		0.258	0.374	0.250	
J0426+0518	0.291	1.305	1.141	0.091	≤1.40	0.414	0.070	0.317	
J0426+2327	0.539	1.586	1.331	1.887	5.78	0.00	1.190	0.00	1.632
J0427+0457	0.335	1.361	1.192	0.457	2.49	0.590	0.336	0.433	0.918
J0437+2037	0.532	2.324	1.992	1.130	≤1.61	0.00	0.486	0.00	
J0431+1731	0.464	1.714	1.457	0.739	3.09	0.00	0.431	0.00	1.198
J0433+0521	0.298	1.159	0.950	0.255	≤1.48	0.795	0.220	0.686	
J0437+2940	0.979	1.320	0.936	4.345	11.98	0.126	3.292	0.095	1.814
J0438+3004	0.952	2.019	1.002	4.586	7.70	0.771	2.271	0.382	2.979
J0439+3045	0.867	2.361	0.745	3.701	9.42	0.00	1.567	0.00	1.964
J0440+1437	0.681	1.659	1.524	0.888	≤1.97	1.230	0.535	0.741	
J0445+0715	0.121	1.044	0.915	≤0.061		0.00	≤0.058	0.00	
J0449+1121	0.504	1.416	1.347	0.476		0.791	0.336	0.558	
J0502+1338	0.564	2.188	1.957	1.324	≤1.90	0.672	0.605	0.307	
J0510+1800	0.328	2.347	1.986	0.092	≤2.00	0.00	0.039	0.00	
J0942-7731	0.336	1.000	0.617	0.837	≤1.50	0.382	0.838	0.382	
J1058-8003	0.152	0.651	0.470	0.147	"	0.371	0.226	0.570	
J1136-6827	0.460	2.407	0.915	0.910	"	0.172	0.378	0.071	
J1145-6954	0.387	1.925	0.998	0.638	"	0.223	0.331	0.116	
J1147-7935	0.300	2.506	0.773	0.040	"	0.00	0.016	0.00	
J1152-8344	0.283	1.088	0.505	0.176	"	0.515	0.162	0.473	
J1224-8313	0.257	0.962	0.563	0.693	"	0.335	0.720	0.348	
J1254-7138	0.282	1.902	0.660	0.102	"	0.00	0.053	0.00	
J1312-7724	0.476	1.257	0.671	0.199	"	0.396	0.158	0.315	
J1550-8258	0.107	0.679	0.416	0.177	"	0.027	0.261	0.039	
J1617-7717	0.091	0.659	0.431	0.043	"	0.045	0.065	0.068	
J1723-7713	0.255	0.834	0.500	1.105	2.40	0.195	1.325	0.234	2.302
J1733-7935	0.139	0.792	0.525	0.041	≤ 1.50	0.00	0.052	0.00	

[1] HI and DNM column densities are from Planck Collaboration et al. (2015) and Remy et al. (2017, 2018)

[2] $N(H_2) = N(HCO^+)/3 \times 10^{-9}$

[3] Integrated J=1-0 CO emission used by Planck Collaboration et al. (2015) and Remy et al. (2017, 2018)

[4] $X_{CO} = N(H_2)/W_{CO}$

observed in the course of this work, chiefly HCO^+, C_2H, and HCN.

Acknowledgements. The National Radio Astronomy Observatory (NRAO) is a facility of the National Science Foundation, operated by Associated Universities, Inc. This work was supported by the French program "Physique et Chimie du Milieu Interstellaire" (PCMI) funded by the Conseil National de la Recherche Scientifique (CNRS) and Centre National d'Etudes Spatiales (CNES). This work is based in part on observations carried out under project number 003-19 with the IRAM 30m telescope]. IRAM is supported by INSU/CNRS (France), MPG (Germany) and IGN (Spain). This paper makes use of the following ALMA data – ADS/JAO.ALMA#2016.1.00714.S

– ADS/JAO.ALMA#2018.1.00115.S ALMA is a partnership of ESO (representing its member states), NSF (USA) and NINS (Japan), together with NRC (Canada), NSC and ASIAA (Taiwan), and KASI (Republic of Korea), in cooperation with the Republic of Chile. The Joint ALMA Observatory is operated by ESO, AUI/NRAO and NAOJ. We thank Isabelle Grenier for providing results of the DNM analysis and we thank the anonymous referee for many helpful remarks. HSL is grateful for the hospitality of the ITU-R and the Hotel de la Cigogne in Geneva during the completion of this manuscript.

References

Cotten, D. L. & Magnani, L. 2013, MN, 436, 1152
Donate, E. & Magnani, L. 2017, MNRAS, 436, 1152
Goldreich, P. & Kwan, J. 1974, ApJ, 189, 441
Gong, M., Ostriker, E. C., & Kim, C.-G. 2018, ApJ, 858, 16
Grenier, I. A., Casandjian, J.-M., & Terrier, R. 2005, Science, 307, 1292
Hu, C.-Y., Sternberg, A., & van Dishoeck, E. F. 2021, ApJ, 920, 44

Table 3. Mean line-of-sight properties and derived quantities

Sample	E(B-V) mag	N(HI) 10^{21} cm^{-2}	N(HI)$_{cl}$ 10^{21} cm^{-2}	2N(H$_2$) 10^{21} cm^{-2}	W$_{CO}$ K-km s^{-1}	N(DNM) 10^{21} cm^{-2}	f$_{H_2}$	f$_{DNM}$	X_{CO}
Galactic anticenter	0.362	1.324	1.119	0.798	5.185	0.268	0.38	0.13	1.93
#	33	33	33	33	9	33	33	33	9
Chamaeleon	0.271	1.282	0.619	0.393	2.400	0.205	0.23	0.12	2.30
#	13	13	13	13	1	13	13	13	1
All LOS	0.336	1.312	0.977	0.684	4.906	0.250	0.34	0.13	1.95
#	46	46	46	46	10	46	46	46	10
$E_{B-V} \leq 0.2$mag	0.131	0.818	0.710	0.168		0.082	0.18	0.08	
#	13	13	13	13		13	13	13	
Lacking HCO^{+1}	0.134	0.918	0.859	≤0.152		0.076	≤0.14	≥0.08	
#	5	5	5	5		5	5	5	
DNM ≤ 10^{20} cm^{-2}	0.273	1.373	0.953	0.539	5.070	0.004	0.28	0.00	1.67
#	17	17	17	17	4	17	17	17	4
CO detected earlier[2]	0.502	1.369	0.928	1.910	4.906	0.204	0.58	0.06	1.95
#	10	10	10	10	10	10	10	10	10
30m CO detected	0.467	1.491	1.197	1.312	2.170	0.318	0.47	0.11	3.02
#	18	18	18	18	18	18	18	18	18
30m W$_{CO}$ >1K-km s^{-1}	0.685	1.690	1.082	2.824	5.522	0.291	0.63	0.06	2.56
#	6	6	6	6	6	6	6	6	6
30m W$_{CO}$ ≤1K-km s^{-1}	0.358	1.391	1.255	0.555	0.494	0.332	0.29	0.17	5.62
#	12	12	12	12	12	12	12	12	12
30m UL ≤1K-km s^{-1}	0.287	1.226	1.107	0.198	<0.140	0.273	0.14	0.19	>7.07
#	10	10	10	10	10	10	10	10	10
Sample	E(B-V) mag	N(HI) 10^{21} cm^{-2}	N(HI)$_{cl}$ 10^{21} cm^{-2}	2N(H$_2$) 10^{21} cm^{-2}	W$_{CO}$	N(DNM) 10^{21} cm^{-2}	f$_{H_2}$	f$_{DNM}$	X$_{CO}$

[1] Limits in this table use 3σ upper limits on undetected quantities
[2] All sightlines detected earlier in CO had W$_{CO}$ >1K-km s^{-1}

Liszt, H. 1997, A&ASS, 124, 183
—. 2021, ApJ, 908, 127
Liszt, H. & Gerin, M. 2023, ApJ, 943, 172
Liszt, H., Gerin, M., & Grenier, I. 2018, A&A, 617, A54
—. 2019, A&A, 627, A95
Liszt, H. S. 2007, A&A, 476, 291
—. 2017, ApJ, 835, 138
Magnani, L., Onello, J. S., Adams, N. G., Hartmann, D., & Thaddeus, P. 1998, ApJ, 504, 290
Planck Collaboration, Abergel, A., Ade, P. A. R., Aghanim, N., Alves, M. I. R., Aniano, G., Armitage-Caplan, C., Arnaud, M., Ashdown, M., Atrio-Barandela, F., & et al. 2014, A&A, 571, A11
Planck Collaboration, Fermi Collaboration, Ade, P. A. R., Aghanim, N., Aniano, G., Arnaud, M., & Ashdown, M. 2015, A&A, 582, A31
Remy, Q., Grenier, I. A., Marshall, D. J., & Casandjian, J. M. 2017, A&A, 601, A78
—. 2018, A&A, 611, A51
Schlegel, D. J., Finkbeiner, D. P., & Davis, M. 1998, ApJ, 500, 525
Wolfire, M. G., Hollenbach, D., & McKee, C. F. 2010, ApJ, 716, 1191

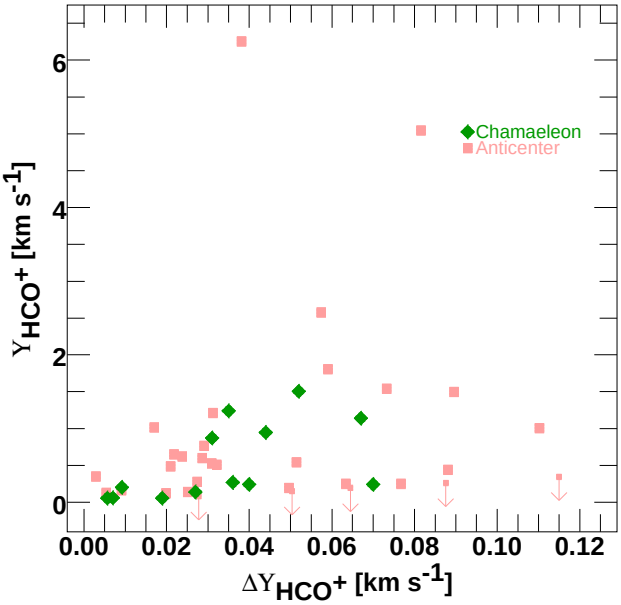

Fig. A.1. Integrated HCO^+ optical depth Υ_{HCO^+} plotted against its rms error. The upper limits along five sightlines not detected in HCO^+ are 3σ.

Appendix A: Statistics of HCO^+ detections

HCO^+ absorption was not detected in five directions, all in the Galactic anticenter sample. Figure A.1 shows Υ_{HCO^+} plotted against its rms error $\Delta\Upsilon_{HCO^+}$, in essence against the strength of the continuum background since all sightlines were observed for the same length of time. The plot shows that even the noisiest sightlines miss relatively small amounts of molecular gas. The bias in the plot, whereby $<\Upsilon_{HCO^+}>$ increases with $\Delta\Upsilon_{HCO^+}$, was to some extent built into the observing to increase the yield. That is, the source selection began with flux-limited samples that would achieve a minimum signal-to-noise ratio on the weakest source, and added 50% additional targets at lower flux S_ν and higher E_{B-V}/S_ν that could be serendipitously observed without a proportionate increase in the required observing time.

Appendix B: Spectra of HCO^+ and CO

Spectra of HCO^+ absorption and CO emission in the 28 directions with detected HCO^+ absorption are shown in Figure B.1. The HCO^+ absorption is the negative-going signal shown in red. The black histogram shows the CO emission. The frequency-switched IRAM 30m CO spectra were delivered only after folding in frequency, preventing a separation of the phases of the frequency-switching cycle using the methods of Liszt (1997). Negative-going features in the CO spectrum are artifacts; only the positive-going CO signal coincident with HCO^+ absorption is interstellar.

Appendix C: Area used to derive large-scale statistics

To derive the statistical distributions shown in Figure 8 and discussed in Section 4.4, we drew a hull around the observed sightlines as illustrated in Figure C.1 and summed over the interior pixels.

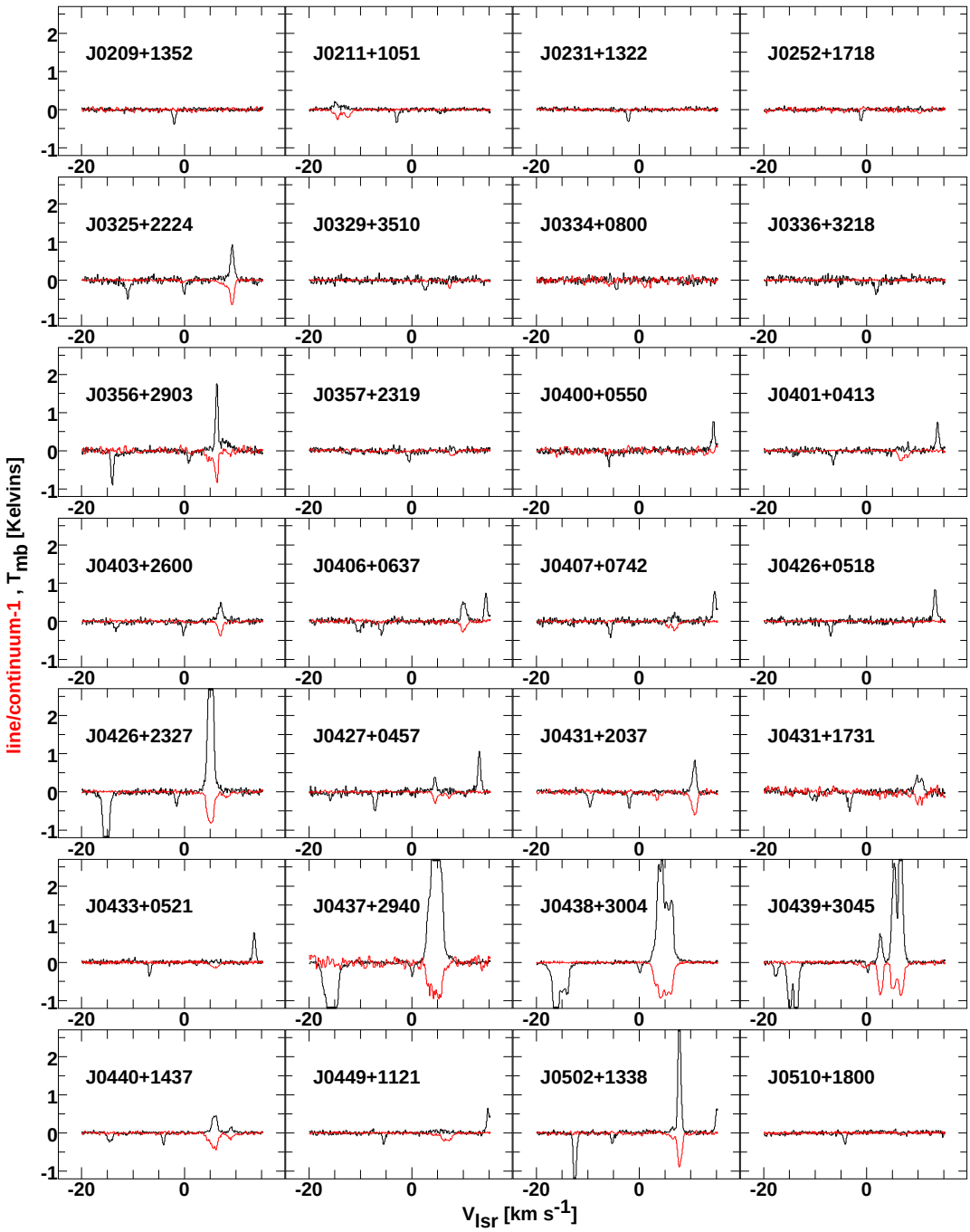

Fig. B.1. Spectra of HCO^+ absorption (red) and CO emission (black) from the Galactic anticenter sample. For an explanation of the appearance of the frequency-switched IRAM 30m emission spectra, see Appendix B.

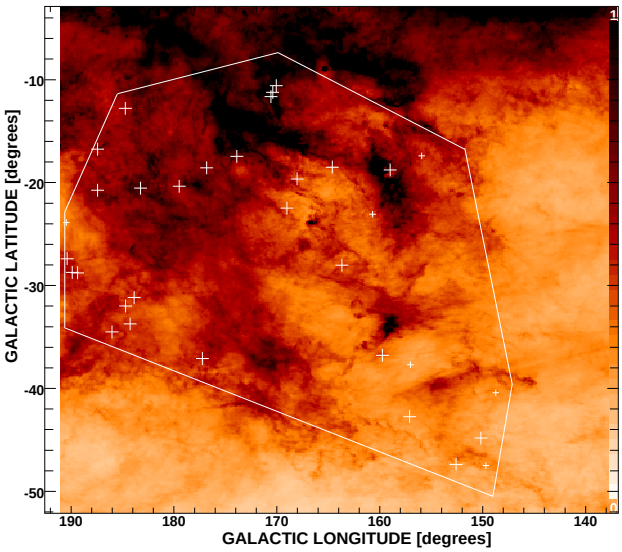

Fig. C.1. As in Figure 1, left, but showing the outlines of an area containing the observed sightlines used to derive large-scale properties of the anticenter region (see Section 4.3).